Materialia 9 (2020) 100523

Contents lists available at ScienceDirect

Materialia

journal homepage: www.elsevier.com/locate/mtla

Full Length Article

Improving the high-temperature ductility of Al composites by tailoring the nanoparticle network

Jinfeng Nie[a], Fenghua Lu[a], Zhaowen Huang[a], Xia Ma[b], Hao Zhou[a], Cai Chen[c], Xiang Chen[a], Huabing Yang[b], Yang Cao[a], Xiangfa Liu[b,*], Yonghao Zhao[a,*], Yuntian Zhu[a,d]

[a] Nano and Heterogeneous Materials Center, School of Materials Science and Engineering, Nanjing University of Science and Technology, Nanjing 210094, China
[b] Key Laboratory for Liquid-Solid Structural Evolution and Processing of Materials, Ministry of Education, Shandong University, Jinan 250061, China
[c] Sino-French Engineering School, Nanjing University of Science and Technology, Nanjing 210094, China
[d] Department of Materials Science and Engineering, North Carolina State University, Raleigh, NC 27695, USA

ARTICLE INFO

Keywords:
Al matrix composites
AlN
Tensile strength
Ductility
Heat resistance

ABSTRACT

Al-matrix composites with networked ceramic nanoparticles have been reported to possess high thermal stability, but their low ductility at high temperatures limits their wide applications. In this study, rotary swaging (RS) was used to modify the network of AlN_p nanoparticles for optimizing the high temperature tensile properties of Al matrix composites. The RS treatment was found to disperse the network structure of AlN_p particles to some extent and to refine the grains of Al matrix, which resulted in high strain hardening and strain rate sensitivity. This not only improved the thermal stability but also increased the uniform elongation from 0.99% to 2.1% at 350 °C. This work provides a new pathway for tailoring the nanoparticle architecture to obtain a desirable strength-ductility synergy for metal matrix composites.

1. Introduction

Al alloys have been increasingly used in automotive engines, aerospace and defense industries for their low density, high specific strength and elastic modulus, and good formability [1–5]. To meet higher requirements on energy-saving and emission-reduction, enhancing the mechanical properties and thermo-stability of Al alloys at elevated temperate is crucial and there have been strong demands for the high strength heat-resistant Al alloys in several industries [6,7]. However, most of the age-hardening Al alloys can work only under 200 °C, because precipitates rapidly coarsen and degrade at higher temperatures [8]. In order to further improve the mechanical properties and meet the requirements in some special fields, ceramic nano-particles (carbides, borides and nitrides, etc.) are used to strengthen the Al matrix, namely particle reinforced Al matrix composites, which show higher thermal stability at temperatures even above 300 °C [9–12].

Many types of ceramic particles, such as AlN and SiC, have high melting points, superior hardness and modulus, and good thermal and oxidation resistance. They can pin the grain boundaries and significantly improve both the room temperature and high temperature strength, but unfortunately also lower the ductility, resulting in a strength-ductility tradeoff [9,13,14]. For example, in our previous study, a network-structured AlN_p reinforced Al composites exhibited the ultimate tensile strength of about 200 MPa at 350 °C, but that comes with a rapid softening behavior and the drastic loss of ductility (less than 3%) [9]. There is however a relentless quest to reach a more superior combination of strength and ductility for advanced applications. A major challenge is to engineer the microstructures to retain ductility for these high-strength metals to achieve a desirable strength-ductility synergy, especially at high temperatures. However, there have been few strategies reported to improve the high-temperature ductility of particle-reinforced Al composites.

It has been reported that the mechanical properties of composites are affected by the particle types, dimensions, volume fractions and the interface structures between the matrix and second phases [15–21]. According to the Hansen-Shtrikman (H-S) bounds theory, adjusting the spatial distribution of the reinforcement and constructing a continuous nanoparticle network structure through the matrix can significantly improve the mechanical properties of composites [22]. Due to the soft matrix surrounded by the hard particles, the accommodating plastic deformation in the matrix grains cannot proceed continuously and will be stopped at the interfaces between the matrix and brittle particle network, leading to the very low work hardening rate. To release the stress concentration at the interfaces, the spatial distribution of the reinforcement particles must be modified and a discontinuous nanoparticle network is proposed to be able to maintain high strength and good ductility [23]. Particle network always forms in-situ during powder metallurgy,

* Corresponding authors.
E-mail addresses: niejinfeng@njust.edu.cn (J. Nie), xfliu@sdu.edu.cn (X. Liu), yhzhao@njust.edu.cn (Y. Zhao).

https://doi.org/10.1016/j.mtla.2019.100523
Received 23 July 2019; Accepted 29 October 2019
Available online 1 November 2019
2589-1529/© 2019 Acta Materialia Inc. Published by Elsevier Ltd. All rights reserved.

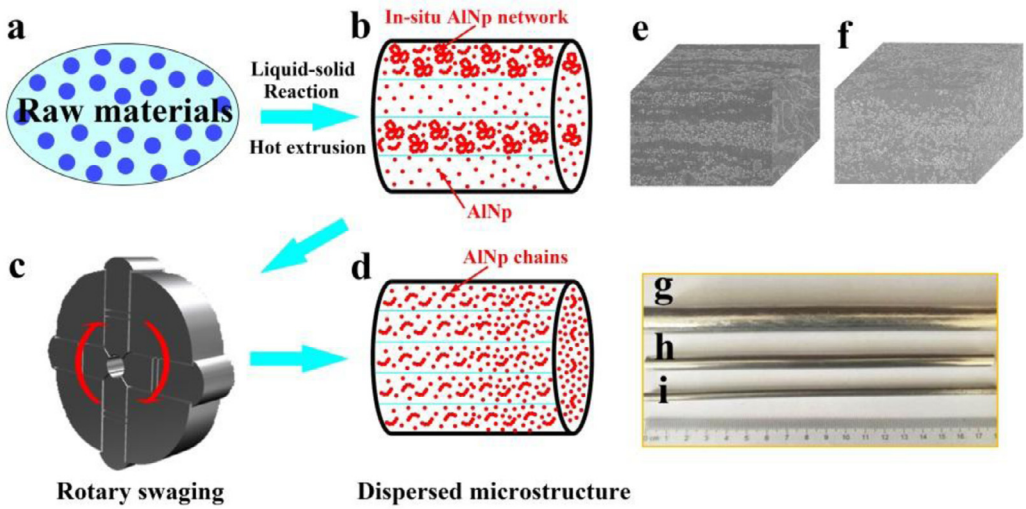

Fig. 1. Schematics showing the preparation processes of the AlN_p/Al composites with different nano AlN_p architectures: (a) mixtures of composite powders; (b) network–structured nano AlN_p reinforced of AlN_p/Al composites after the liquid-solid reaction and hot extrusion; (c) rotary swaging process of the extrudes sample; (d) the dispersed microstructure of the composites; (e and f) SEM images shows the particle distributions in EXT and RS0.2 samples; (g-i) the appearances of the three samples of EXT, RS0.2 and RS0.6.

which was hardly affected by the following heat treatment and hot extrusion processes with low strain deformation. Furthermore, there are few studies about tailoring the architecture of the composites to regulate the mechanical properties of Al-based composites.

Severe plastic deformation (SPD) techniques, including equal channel angular pressing [24] and high pressure torsion [12], can be employed to tailor the architecture of the reinforcement particles and break the ceramic particle network to some extent to accommodate plastic deformation in the metal matrix grains. However, these SPD processes either require high plasticity of the sample or are limited in work-piece sizes, making it difficult to be widely applied in production of bulk composites. A new strategy for processing large bulk work pieces is needed to optimize the structure of bulk nanoparticle reinforced composites. Rotary swaging (RS), as a relatively new SPD processing technique, can be used to prepare bulk samples including rods, tubes and wires through the repeated action of rotating split dies and then achieves microstructural and properties optimization [25,26]. Some of the advantages of rotary swaging include short cycle times, good surface finishes and tight size tolerances [27]. In this study, RS was employed to tailor the spatial distribution of the nanoparticles in bulk networked AlN_p reinforced Al composites to improve the tensile ductility at elevated temperatures.

2. Experimental

2.1. Fabrication of AlN_p/Al composites

Fig. 1 schematically shows the fabrication process of the AlN_p/Al composites in the present study. Commercial pure Al powders (99.7%, all compositions quoted in this work are nominal values in mass fractions unless otherwise stated) with an average particle size of ~20 μm and nitride plastid powders (99%) with an average particle size of ~2 μm were used, as reported in our previous work [9]. As shown in Fig. 1a, mixtures of composite powders, containing the Al powders with nitride plastid powders, were prepared first. Network–structured nano AlN_p reinforced of AlN_p/Al composites (Fig. 1b and e) were fabricated by liquid-solid reaction and the following hot extrusion reported in the prior study [28], which is named as EXT. The mass fraction of AlN_p was 8.2 wt.% and the volume fraction was estimated to 6.6 vol.% on the basis of the atomic fraction of the major element in the base metal and nanoparticles. After that, the samples were subjected to RS at room temperature with equivalent strains of about 0.2 and 0.6 (named as RS0.2, RS0.6), as shown by Fig. 1c, respectively. The equivalent von Mises strain, ε_{eq}, is calculated using the relationship [29,30]:

$$\varepsilon = 2\ln\frac{D_0}{D} \tag{1}$$

where D_0 and D are the diameters of the sample before and after RS, respectively. The network structure of the nano AlN_p is supposed to have been deformed and damaged to a certain extent after RS to form a more homogenous microstructure with dispersed AlN particles and particle chains, as shown in Fig. 1d and f. Fig. 1g–i show the specific pictures of the AlN_p/Al composite rods by EXT and RS treatments with different deformation strain of 0.2 and 0.6, respectively, and also indicate the advantages of RS samples with smooth surfaces.

2.2. Microstructure characterization

The phase identification and microstructural characterizations of the AlN_p/Al composites were performed using X-ray diffraction (XRD, Rigaku D/max-rB), scanning electron microscope (FESEM, Quanta 250F, worked at 15 kV) equipped with Oxford energy dispersive X-ray spectrometer (EDS), electron backscattered diffraction (EBSD, Zeiss Auriga, using a step size of 0.15 μm) and transmission electron microscope (TEM TECNAI 20). The samples for EBSD mapping were mechanically polished and then electro-chemically polished in a mixed solution of 10% perchloric acid and 90% ethanol with a voltage of 20 V for 15 s at −20 °C. All EBSD data were analyzed using the Channel 5 software and Atex software [31]. A TECNAI G2 200 transmission electron microscope (TEM) with a spherical aberration corrector under the objective lens operated at 300 kV was used to analyze the interface structure of the nanoparticles and Al matrix. High-angle annular dark-field (HAADF) scanning transmission electron microscopy (STEM) and selected area electron diffraction (SAED) were employed to characterize nano-sized structures. Thin foils for TEM observations were prepared with mechanical polishing to the thickness of 25 μm. The specimens were finally polished by ion beam using Gatan 691 precision ion polishing system (PIPS).

2.3. Tensile testing

The tensile properties of the above composites were conducted according to the ASTM E0021-03A standards to evaluate the mechanical properties at the elevated temperature of 350 °C. The specimens were dogbone-shaped with 5 mm in diameter and 40 mm in original

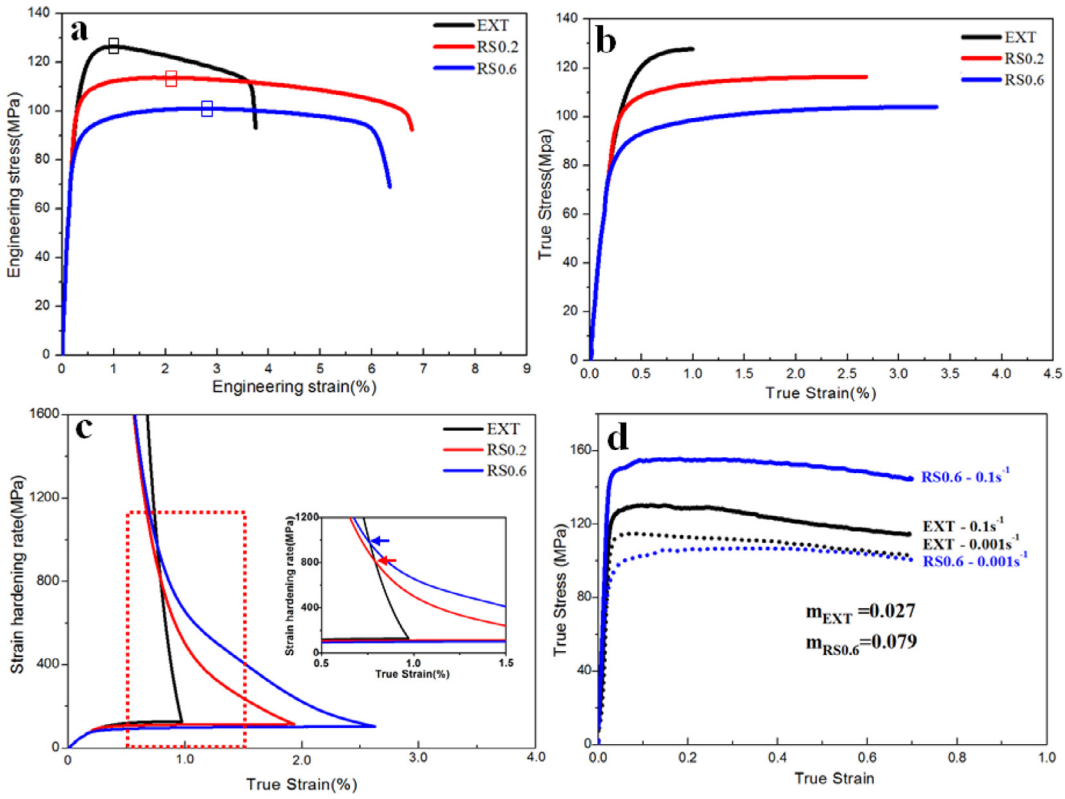

Fig. 2. Tensile and compression properties of AlN_p/Al composites at 350 °C before and after RS treatment: (a) engineering tensile stress-strain curves; (b) true tensile stress-strain curves showing the enhanced ductility; (c) strain hardening rate ($\Theta = d\sigma/d\varepsilon$) curves indicating the better hardening rate retention in the RS treated samples; (d) true compressive stress-strain curves at different strain rates (as marked) showing the higher strain rate sensitivity in the RS treated sample.

Table 1
Mechanical property of the EXT and RS treated AlN_p/Al composites at 350 °C.

Samples	YS/MPa	UTS/MPa	UE/%	EI/%
EXT	120	126	0.99	3.38
RS0.2	107	113	2.1	6.43
RS0.6	91	101	2.75	5.78

gauge length. Tensile tests were carried out by first holding at 350 °C for 30 min, and then tension at a strain rate of $0.8 \times 10^{-3} s^{-1}$ with strain measured by a standard video extensometer. For each sample, the average tensile strength at 350 °C was acquired from three specimens.

3. Results

3.1. Mechanical behavior of the AlN_p/Al composites at 350 °C

Fig. 2 shows the high temperature mechanical properties of the AlN_p/Al composites at 350 °C before and after RS. Fig. 2a displays the engineering tensile stress-strain curves with and without RS treatments. Detailed tensile strength and ductility values are given in Table 1. The engineering stress-strain curve for the sample EXT shows that the yield strength is ~120 MPa and the ultimate tensile strength (UTS) is ~126 MPa, with a corresponding uniform strain of only ~0.99%. That is, after reaching UTS, sample EXT becomes unstable (i.e. necking) immediately after yielding and shows significant strain softening. The stress dropped rapidly and decreased linearly until fracture and the elongation to failure is less than 3.4%. After RS treatment, the engineering stress-strain curve for sample RS0.2 exhibited a flat plateau until reaching UTS of ~113 MPa, and the uniform strain reaches ~2.1% (red square on the curve). The UTS is comparable with that of the sample EXT and decreased by only 10%. However, the curvature in this region indicates a more uniform elongation, which increased by ~112%. The elongation to failure of this sample is close to 6.5%, indicating that its high-temperature ductility at 350 °C is enhanced significantly after RS processing. UTS of sample RS0.6 is about 101 MPa and its uniform elongation is up to ~2.75%. Compared to the properties of sample EXT, uniform elongation of sample RS0.6 increased by as high as 178% and the UTS reduced by 20%, which is consistent with those of sample RS0.2. Therefore, the ductility of the AlN_p/Al composites at the elevated temperature of 350 °C was significantly increased by RS processing, although the strength has been scarified to some limited extents.

The high-temperature true tensile stress-strain curves of the three samples at 350 °C are given in Fig. 2b, and the uniform elongation of AlN_p/Al composites after RS treatments was increased significantly, agreeing with the aforementioned results. The onset of localized deformation, e.g. necking instability, occurs due to the low work hardening behavior of a materials, according to Hart criterion [32,33]

$$\frac{d\sigma}{d\varepsilon} \leq (1 - m)\sigma \tag{2}$$

where σ is the true stress, ε is the true strain and m is the strain rate sensitivity (SRS). m is not sufficiently high for ultrafine grained structured and nano-structured metals ($m < 0.05$) at room temperature [34–37], but increases significantly at high temperature. Higher m helps with sustaining homogenous deformation.

Fig. 2c shows the strain hardening ($\Theta = d\sigma/d\varepsilon$) curves of the three samples, which decreased rapidly with increasing strain. Interestingly, the RS0.2 and RS0.6 samples have a slower decrease in Θ than the as-extruded one with strain. As a result, when the strain is larger than a critical value of ~0.75% (Fig. 2c, indicated by the arrows in Inset), Θ values of RS0.2 and RS0.6 samples surpass that of the as-extruded one, which indicates a better Θ-retention and an improved strain hardening in the RS treated samples. More importantly, with further increase of strain, the strain hardening rates of RS0.6 also become much higher

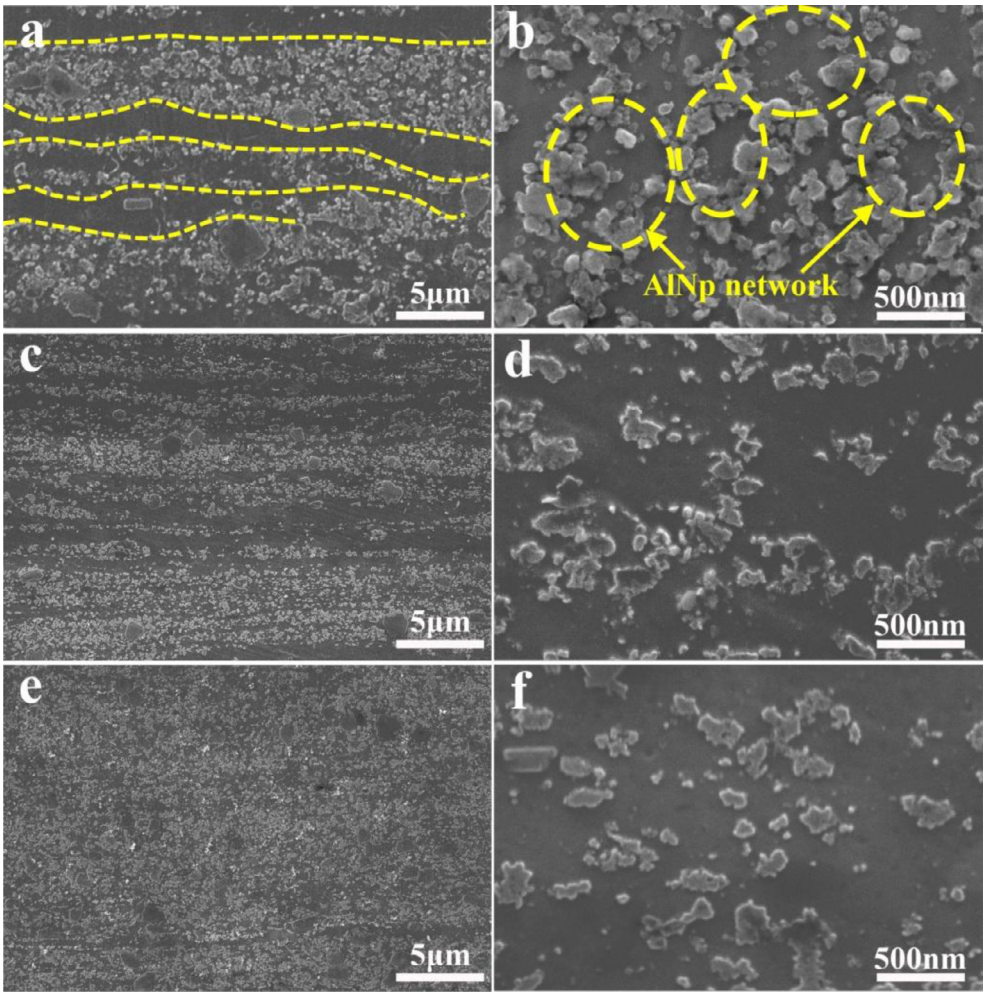

Fig. 3. Microstructures of different AlN_p/Al composites along the longitudinal direction: (a) the heterogenous distribution of AlN_p in EXT sample; (b) the network structure of AlNp seen at a higher magnification; (c, d) the distribution of AlN_p in RS0.2 sample at lower and higher magnification; (e) the dispersive distribution of AlN_p in RS0.6 sample. and (f) the dispersed AlN_p in the matrix.

than that of RS0.2, indicating that Θ-retention is also improved with increased RS deformation. It is also noted that the critical strain value is lower for RS0.6 than RS0.2. Thus, the strain hardening rates of the composites were enhanced by RS at a higher strain. To our knowledge, the good Θ-retention behavior at high temperature in the Al based alloys realized by RS treatment is revealed for the first time and is inherent to the regulated heterogenous microstructure in the materials [38,39].

In addition, to evaluate the SRS at high temperature and the contribution of strain rate hardening on the enhanced uniform deformation, high temperature (350 °C) compressive tests of the composites before and after RS treatment were carried out at the strain rates of 10^{-3} and 10^{-1}, respectively. Fig. 3d shows the flow stress variation of the composites with the compressive strain, which is compared with tensile stress variation of the samples before and after RS. The slight decrease of flow stress is similar with the variation trend of the tensile strength at a quasi-static strain rate. However, it is noted that the flow stress of the RS0.6 sample is increased significantly at a higher strain rate of 0.1 s^{-1}, indicating the distinct SRS. m can be calculated according to the following equation [34]

$$m = \frac{d\log\sigma}{d\log\dot{\varepsilon}} \tag{3}$$

where σ is the steady state true flow stress at a given strain rate $\dot{\varepsilon}$. The value of m is not constant and varies with the microstructure features such as grain size and second phase distribution. For face-centered cubic metals, m increases significantly with decreasing grain size [40], due to the enhanced dislocation-grain boundary (GB) interactions [41]. Moreover, it is known that GB sliding plays an important role in the high-temperature deformation [42], which may further increase the SRS. The value of m for the composite is estimated based on Fig. 3d and it is increased from 0.027 to 0.079 at 350 °C (a high homologous temperature T/T_m ~0.67), both of which are much higher than that of Al composite at room temperature ($m \approx 0.001$–0.02) [43]. This indicates (i) the enhanced GB sliding behavior at 350 °C, (ii) reduced grain size of Al matrix (as revealed below) and/or further enhanced GB sliding after RS treatment.

Corresponding to the enhanced strain rate dependence, there is also a pronounced temperature dependence, arising from the thermal activated deformation mechanisms controlling the plastic flow. The significant strain rate dependence of strength on strain rate and temperature always shows a reduced activation volume, which also benefits to the ductility of the materials. Thus, the activation volume v is calculated using the following equation

$$v = \sqrt{3}k\mathrm{T}\frac{d\ln\dot{\varepsilon}}{d\sigma} \tag{4}$$

Where k is the Boltzmann constant, T the absolute temperature, σ the uniaxial flow stress and $\dot{\varepsilon}$ the strain rate [40]. The calculated activation volume has been decreased significantly from 191.5b^3 for EXT sample to 57.3b^3 for RS0.6 at 350 °C, which indicates the AlN_p/Al composite has a stronger dependence on the strain rate and have a lower activation volume after RS treatment. It is reported that the ultrafine grained metals possess higher GB diffusion than their coarse-grained counterparts [43,44]. Especially, GB sliding at high temperature leads to higher strain rate sensitivity, which benefits the ductility. Therefore, both higher strain hardening and higher strain rate sensitivity contributed to the enhanced ductility after RS treatment.

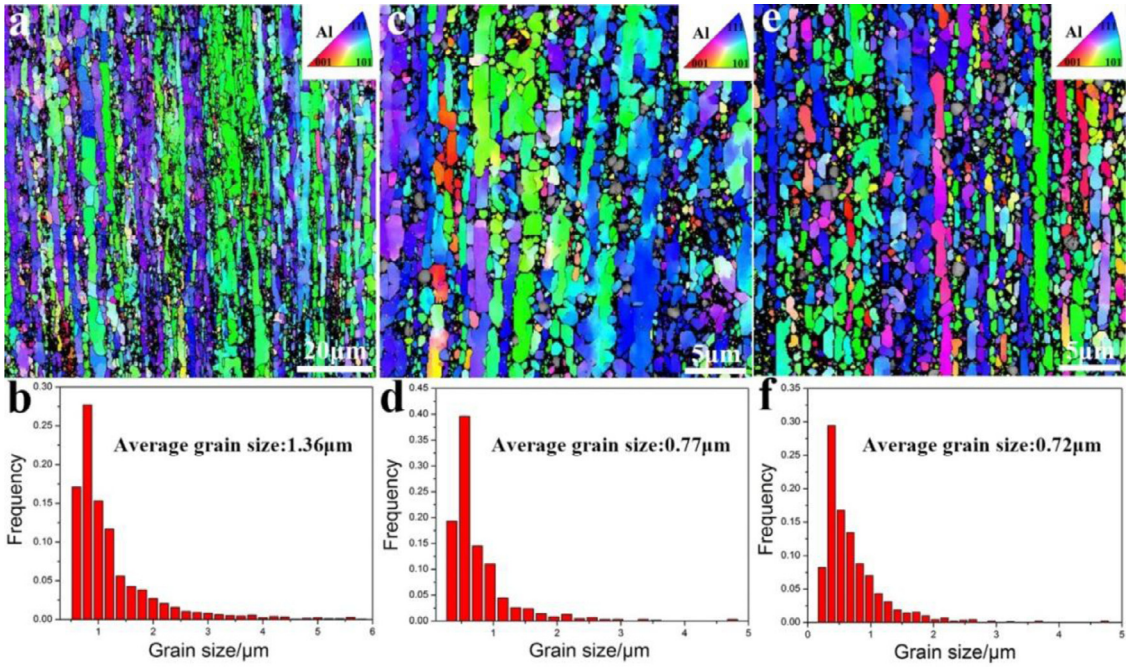

Fig. 4. EBSD analysis of the AlN_p/Al composites at the longitudinal section: (a, b) inverse pole figure (IPF) map of α-Al grains of sample EXT and the grain size distribution; (c, d) IPF map of α-Al grains of RS0.2 sample and the grain size distribution; (e, f) IPF map of α-Al grains of RS0.6 sample and the grain size distribution.

3.2. Microstructural characterization of the AlN_p/Al composites

To find the reason for the enhanced strain hardening and strain rats hardening of the composites at 350 °C, the microstructures of the EXT and RS treated composites including the AlN_p distributions were investigated. Fig. 3 shows the morphology and distribution of AlN_p. From Fig. 3a, it can be seen that a heterogenous microstructure was formed along the longitudinal direction in the EXT sample during the extrusion process, which consists of reinforcement particle rich layer with a size of about 1.5~7.5 μm and lamellar Al grain strips with sizes of about 2~3.5 μm. The interfaces between particle rich zone and particle lean zone are also marked by the yellows lines in Fig. 3a. Higher magnification image (Fig. 3b) indicates that most of the AlN particles are inter-connected, forming a network structure observed in our previous work [9]. After RS treatment for an equivalent strain of 0.2, the original lamellar distribution of AlN_p was changed (Fig. 3c), and a more homogenous structure was attained. Besides, the particle-deficient area was reduced significantly in sample RS0.2 compared with that in EXT sample and the particle interspace increased correspondingly at a higher magnification (Fig. 3d), indicating that the original network structure was broken to some extent during RS deformation. However, most of particles still connect with each other and form AlN_p chains at a small scale of about several hundred nanometers in the matrix. With further increase of the deformation strain, most of the AlN particles were dispersed much more homogenously in the Al matrix, as shown in Figs. 3e and f.

Furthermore, the influence of RS processing on the grain structure of Al matrix was investigated by EBSD analysis. Figs. 4a–f show the inverse pole figure (IPF) maps and grain size statistic distributions of α-Al grains in the composites before and after RS treatment. As shown in Fig. 4a, most of the α-Al grains in the as-extruded sample have long elongated structure with a large width range of submicron to over 4 μm, due to the heterogeneity of network-structured AlN_p and is consist with the SEM images shown in Fig. 3a. Besides, a small amount of recrystallized grains with equiaxed morphologies can be found. It can be seen that the dark areas have not been indexed, which are occupied with AlN particles in the matrix. The grain size distribution of α-Al matrix is shown in Fig. 4b and has an average grain size of ~1.52 μm. Fig. 4c gives the grain structures of sample RS0.2, which shows that the elongated grain width range decreased, indicating refinement of the large elongated grains during the RS. The corresponding grain size distribution of RS0.2 is shown in Fig. 4d, and most of the coarse elongated grains were refined to submicron scale and has a much smaller mean size of ~0.8 μm than that of EXT. With increasing RS strain up to 0.6, the average grain size further decreased to ~0.76 μm (Figs. 4e and f). According to the above results, it can be concluded that the coarse elongated α-Al grains were refined significantly along with homogenous dispersion of AlN_p during the RS process.

Fig. 5 shows the distribution and fraction of recrystallized grains in the three composites. Compared with the EXT sample (Fig. 5a), it can be seen that the fraction of recrystallized grains was slightly increased from 14.2% to 14.7% in the RS0.6 sample (Fig. 5c). However, for the RS0.2 sample the fraction of the recrystallized grains decreased to 7.5% and the fraction of deformed grains increased from 69.8% to 84.4% (Fig. 5b). Thus, the fully recrystallized grains in the EXT sample were further deformed after RS treatment for a low strain of 0.2. Besides, it is noticed that the fraction of the LAGBs (misorientation angle of 2–15°,) is decreased from 62% to 57% and 38%(Figs. 5d, e and f), indicating the evolution of LAGBs to HAGBs (misorientation angle exceeding 15°) has been occurred during the RS deformation process. Therefore, most of the equiaxed grains are formed by the evolution of LAGBs during the plastic deformation for a low strain of ~0.2 and the fraction of deformed grains increased in the RS0.2 sample. With the further increase of the deformation strain to 0.6, dynamic recrystallization started, and then the fraction of recrystallized grains increased in the RS0.6 sample.

TEM was used to analyze the microstructure of AlN_p/Al composites at higher resolution than EBSD. Fig. 6a shows the TEM micrographs of sample EXT, in which elongated coarse α-Al grains and the particle-rich strips consisting of nano-scale AlN particle clusters, evidenced by the corresponding diffraction pattern shown in the inset of Fig. 6a. At a higher magnification (Fig. 6b), it can be seen that either the isolated AlN particles or the network-structured AlN particles are located both at the GBs and in the interior of α-Al grains. Due to the effective pinning effects on the dislocations by nano AlN particles, the matrix α-Al grains in the particle rich zone are also refined significantly to submicron scale during the hot extrusion process. After RS treatment for dif-

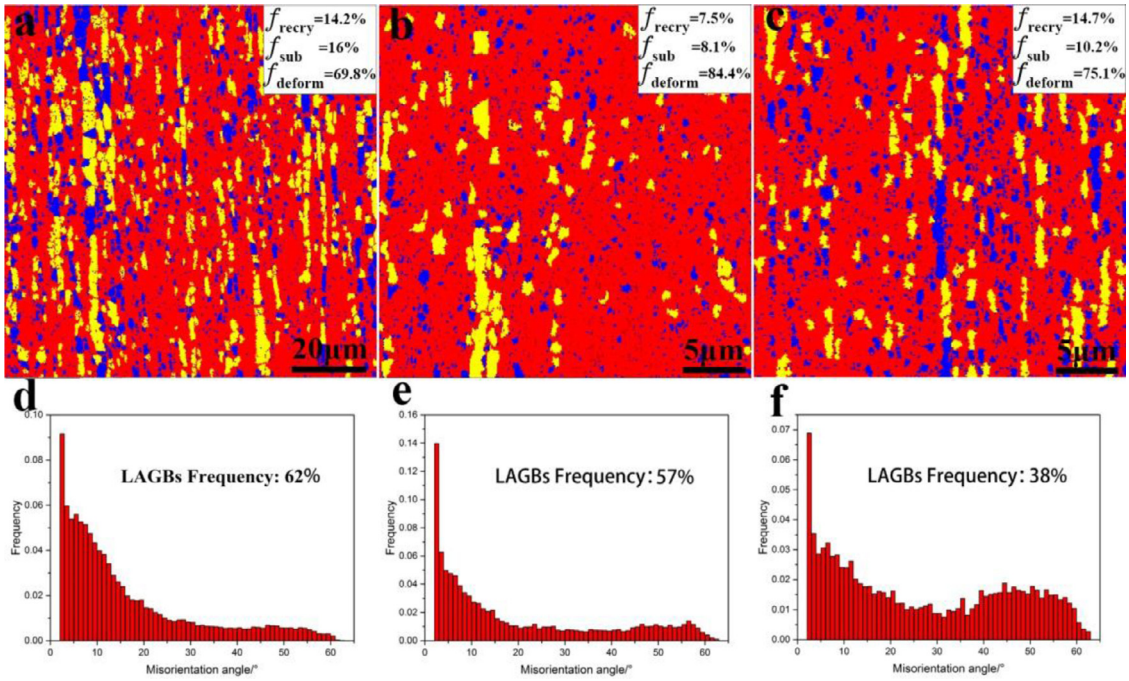

Fig. 5. Recrystallized fraction illustrations (fully recrystallized grains are shown in blue, substructured grains in yellows, and severely deformed grains in red) of the three different AlN_p/Al composites and the corresponding misorientation angle distribution: (a, d) EXT sample; (b, e) RS0.2 sample; (c, f) RS0.6 sample. (For interpretation of the references to colour in this figure legend, the reader is referred to the web version of this article).

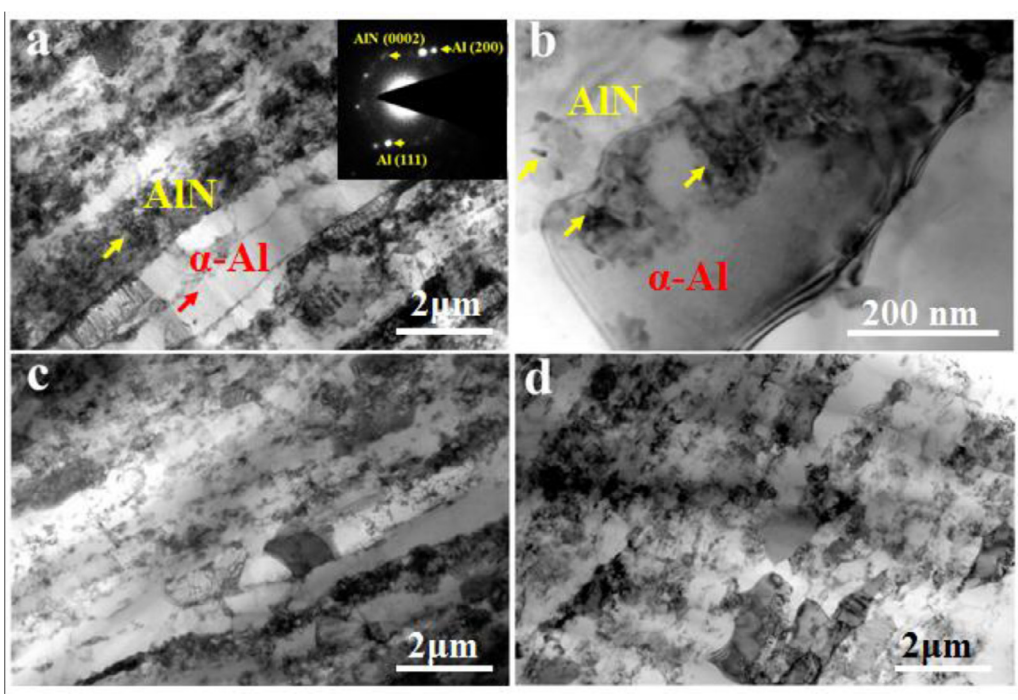

Fig. 6. Typical TEM images of different AlN_p/Al composites: (a) showing the heterogenous distribution of AlN particles and the lamellar α-Al grains in EXT sample; (b) the isolated AlN particles or the network-structured AlN particles located both at the GBs and in the interior of α-Al grains in EXT sample; (c) the more dispersed distribution of AlN_p and refined α-Al grains in RS0.2 sample; (d) the dispersive distribution of AlN_p and refined equiaxed α-Al grains in RS0.6 sample.

ferent strain of 0.2 and 0.6, the severe AlN particle agglomerates were dispersed to a lager extent during the plastic deformation and a much more homogenous structure was obtained, as shown in Figs. 6c and d. It also suggested that the original submicron-sized network-structure of AlN particles was broken to some extent. Meanwhile, most of the elongated α-Al grains were refined and an ultrafine-grained structure was formed in the matrix.

Fig. 7 shows the HRTEM images of the AlN_p/Al composites of sample RS0.2. Nano scale AlN particle clusters are distributed in the matrix (Fig. 7a), which indicates that some submicron sized AlN networks in the matrix were broken and dispersed during RS treatment. While some nano-scale network structure was reserved as shown by the HADDF-STEM image (Fig. 7b) and the AlN particles connect with each other to form three-dimensional particle chains throughout the matrix. Accord-

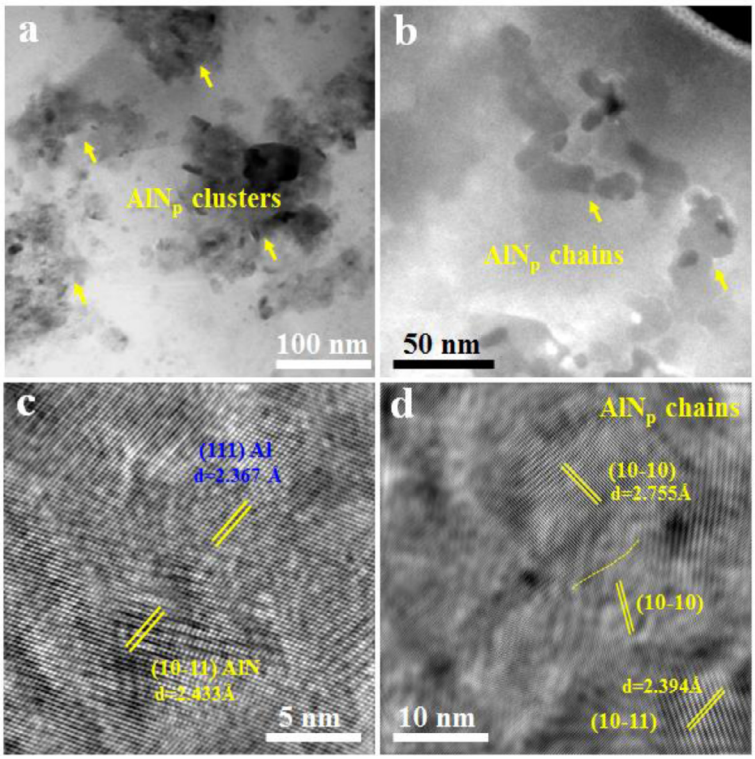

Fig. 7. HRTEM analysis of AlN_p/Al composites of sample RS0.2: (a) the dispersive AlN clusters with size ~100 nm; (b) HADDF-STEM image showing the nano-scale AlN network-structure; (c) lattice fringe images showing the good atomic bonding between AlN and Al matrix; (d) lattice fringe image showing the good atomic connection in AlN_p chains.

ing to the clear lattice fringe image of AlN and Al grains as displayed in Fig. 7c, AlN particles embed in the Al matrix and they share an orientations relationship of $(10–11)_{AlN}$ //$(111)_{Al}$, indicating the coherent interface exists between AlN_p and Al matrix. Fig. 7d shows the lattice fringe images of three connected AlN particles in the Al matrix and the interfaces are clean and well bonded without any other compounds. It can be concluded that the good atomic bonding between the AlN_p and the matrix plays the crucial role in the enhancement of the high-temperature strength.

4. Discussion

4.1. Effect of particle's spatial distribution on high-temperature strength of the composites

Based on the above results, tailoring the AlN_p network structure by RS has improved the ductility of the composites along with slight sacrifice of the tensile strength at high temperatures. In this section, the mechanism of this observation will be discussed.

It is known that the Hashin-Shtrikman (H-S) bounds theory can be used to analyze the effect of AlN network structure on the variation of strength for the composites. The totally continuous network boundary can be considered the same as the one with H-S upper boundary as shown in Fig. 8 [22,23], meanwhile, a homogenous microstructure is similar with the one with H-S lower boundary. For the elastic modulus (E) of an isotropic two-phase composite, it can be expressed as [23]:

$$E_{HS-Upper} = \frac{E_r(E_rV_r + E_m(2 - V_r))}{E_mV_r + E_r(2 - V_r)} \tag{5}$$

$$E_{HS-Lower} = \frac{E_m(E_m(1 - V_r) + E_r(1 + V_r))}{E_r(1 - V_r) + E_m(1 + V_r)} \tag{6}$$

where $E_{HS\text{-}Upper}$ and $E_{HS\text{-}Lower}$ are the values of upper and lower bounds, respectively; E_m and E_r are the E values of Al and AlN, respectively. V_r is the volume fraction of AlN.

For the EXT sample, the existence of AlN_p network provides great reinforcing effects as shown in Fig. 2, which is close to the H-S upper

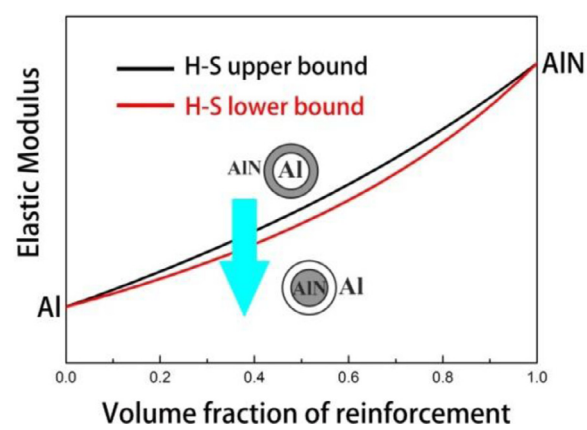

Fig. 8. The Hashin-Shtrikman (H-S) bounds for the elastic modulus of composites [23].

boundary. The high strength arises from the synergistic strengthening effects of the in-situ nano AlN_p and the 3D network structure of AlN_p. The good interfacial bonding in AlN_p/Al composite helps with effective stress transfer. Such kind of architectures show good resistance to dislocation slip, and the stress required for the dislocations to pass through the particles barriers is high. The composite yields only when the stress is sufficiently high for the network barriers. Considering another ideal case of the homogenous microstructure, it is supposed that AlN particles are distributed in the matrix homogenously, and the corresponding strength reaches to H-S lower boundary. In the present experiment, with the proceeding of plastic deformation, the AlN_p network evolves to become discontinuous. Meanwhile, the corresponding strengthening effect dominated by AlN_p network structure decreases to a certain extent.

It is also shown that the matrix grains are refined significantly during the RS treatment. And the fraction of deformed grains and the recrystallized ones increased as shown in Figs. 5e and f, indicating the partial recrystallization occurred during the RS treatment. It is known that atomic diffusion at grain boundaries are easily occurred at high tem-

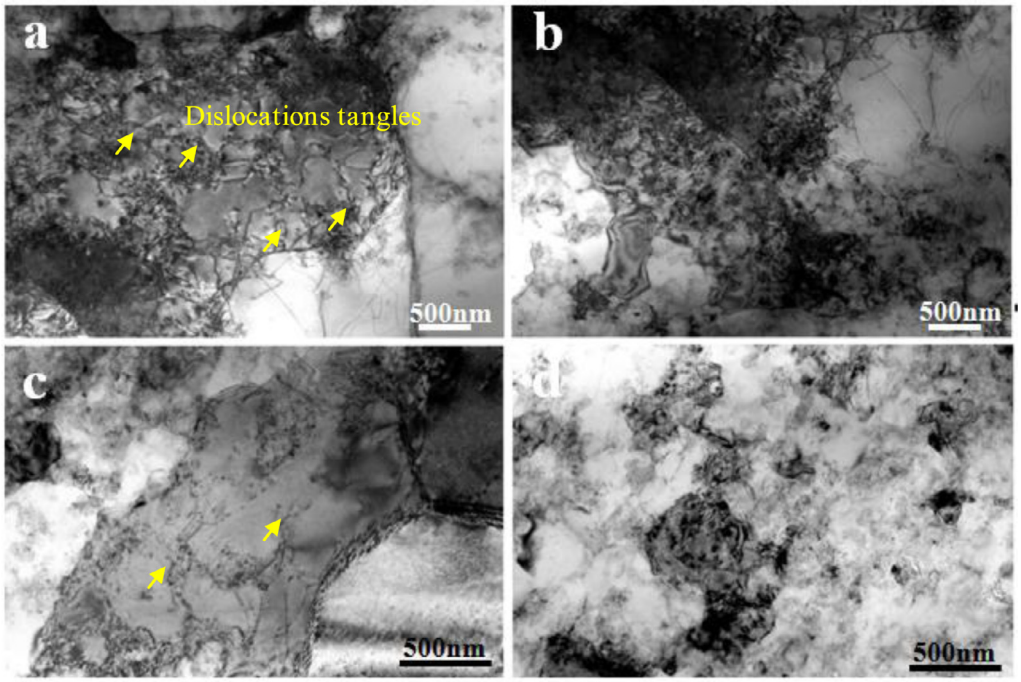

Fig. 9. Typical TEM observation of the microstructure of the composites after tensile at 350 °C: (a, b) showing amounts of accumulated dislocations in EXT sample induced by the AlN_p net-work; (c, d) the dislocations pinned by the isolated AlN_p in sample RS0.2, the yellow arrows indicate the dislocation tangles in the α-Al grains. (For interpretation of the references to colour in this figure legend, the reader is referred to the web version of this article).

perature leading to the reduced strength of grain boundary. Therefore, it can be concluded that the partial recrystallization also contribute to the reduction of high temperature tensile strength. It is considered that the thermal stability and strength of AlN particle are much higher than those of Al matrix at 350 °C, the strengthening effect of AlN particles and chains is much higher than that of matrix, which can still behave a relatively high strength at the present temperature. Thus, the tensile strength of the composites was reduced slightly.

Both samples before and after RS treatment had a high tensile strength at 350 °C, which is much higher than the recrystallization temperature of Al In order to reveal the strengthening mechanism, distributions of accumulated dislocations in the samples were observed by TEM after tensile test at 350 °C (Fig. 9). It can be seen that dislocations tangles indicated by the yellow arrows accumulated in α-Al grains due to the pinning effect of the AlN particles (Fig. 9a), whereas in the AlN_p free zones, the dislocation density is much lower (Fig. 9b). Although the integrated network-structure of AlN_p was changed to some extent during RS deformation, a large number of dislocations still can be found in the matrix grains after tension at 350 °C (Figs. 9c and d), which is supposed to be induced by the isolated AlN particles and the small sized AlN chains as evidenced in Fig. 7b. These results indicate that the AlN_p /Al composites can achieve excellent high-temperature strength by hindering the movement of dislocations and their accumulation, which arises from the hierarchical spatial distribution of AlN_p throughout the Al matrix.

4.2. Effect of microstrucre variation on the high-temperature ductility

Generally, the common strengthening strategies for structural materials are accompanied by a sacrifice in ductility, known as the strength-ductility trade off dilemma [45]. While the lack of strain hardening and the strain rate sensitivity leads to the rapid softening mechanism. In aluminum alloys, nanoscale particles have been shown to play a crucial role in breaking this barrier [46,47]. In the present work, it has been shown that the uniform elongation of composite after RS improved remarkably in spite of a slight reduction of strength (Fig. 2). To better understand the improvement of ductility at high temperatures, the α-Al grain structures and the average grain sizes of the composite sample near the fracture after tensile tests were further characterized by EBSD (Fig. 10). As shown in Fig. 10a, most of the refined elongated grains can be still seen in sample EXT owing to the excellent impediment of AlN_p, and the average grain size increased slightly from 1.36 μm to 1.42 μm. It is also noted that some α-Al grains grow abnormally to ~8 μm during the high-temperature tensile test as shown by the black arrows in Fig. 10a, indicating the non-uniform deformation during the tensile test. However, when the architecture of network-structured AlN_p was tuned by RS treatment, the grain growth in the matrix was more uniform and the abnormal large grains were not observed as shown in Figs. 10c and e. Meanwhile, the average grain sizes of sample RS0.2 and RS0.6 increased slightly from 0.77 to 0.80 μm, from 0.72 to 0.76 μm, which indicates the good thermal stability of the α-Al grains induced by nano AlN particles and its architecture.

Besides, the recrystallized grains in the EXT, RS0.2 and RS0.6 samples were analyzed as shown in Figs. 11a, b and c, respectively. Compared with the recrystallized grain distributions in the composites before tensile tests in Fig. 5, it can be seen that the fraction of recrystallized grains in the RS0.2 and RS0.6 samples were increased significantly as shown in histogram of Fig. 11d. Therefore, it can be concluded that recrystallization has been occurred during the high temperature tensile tests. While, it is noticed that the fraction of recrystallized grains in the EXT sample is decreased, but the fraction of substructured grains is increased significantly from 15.9% to 46.4%, indicating that recovery is dominated in the EXT sample during the high temperature tensile tests.

It is known that the strain localization promotes the final failure during tensile test. In order to observe the strain distribution and strain localization directly in the three samples after tensile test, Kernel average misorientation (KAM) maps of the three samples were obtained (Fig. 12) based on the EBSD data in Fig. 10, which indicated the local misorientations of neighboring grains. Generally speaking, the larger strain deformation the local region is subjected to, the higher the misorientation angle appears. As shown in Fig. 12, the red correspond to the highest stress values, whereas the blue is associated with the lowest stress values. As

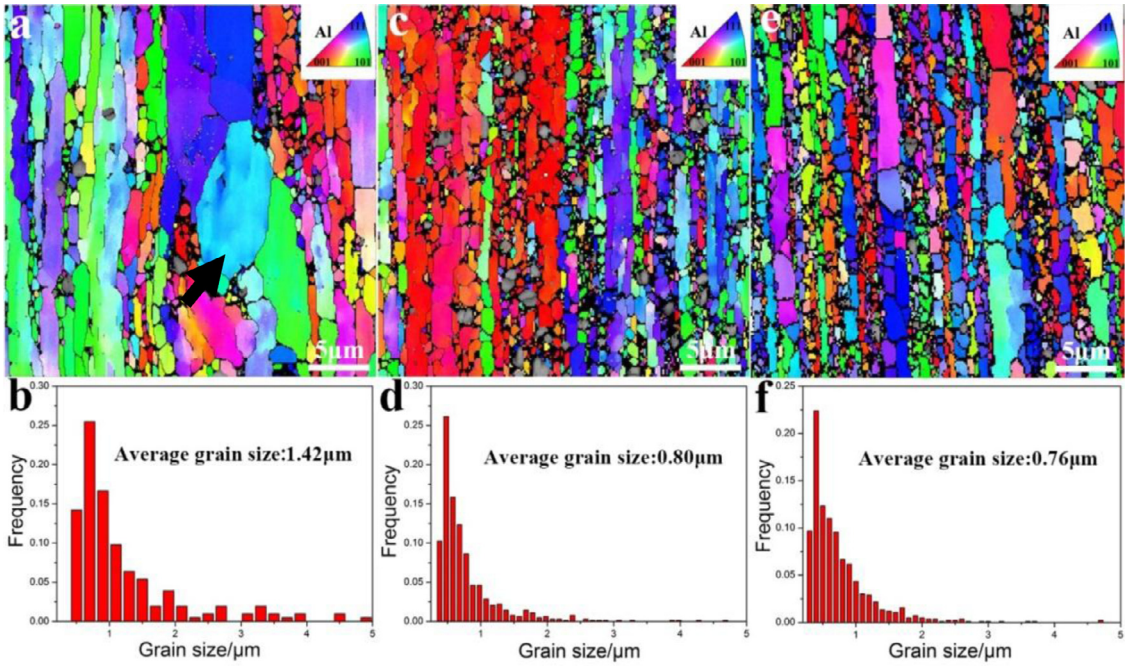

Fig. 10. EBSD analysis of α-Al grains in the composites near the fracture surface after tensile test at 350 °C: (a, c, e) IPF maps of α-Al grains at longitudinal section of EXT, RS0.2 and RS0.6, respectively, the arrow indicates the abnormal grain growth of α-Al during the high temperature tensile test; (b, d, f) the corresponding grain size distribution.

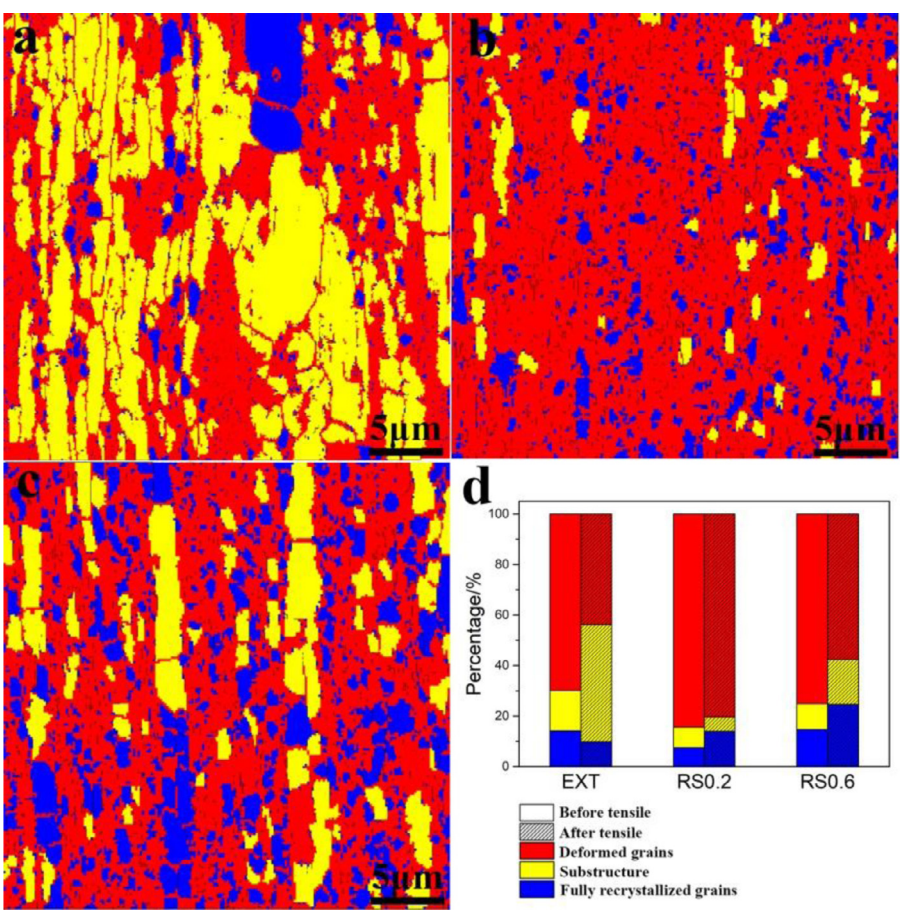

Fig. 11. Recrystallized fraction illustrations (fully recrystallized grains are shown in blue, substructured grains in yellows, and severely deformed grains in red) of the three different AlN_p/Al composites after 350 °C tensile tests: (a) EXT sample; (b) RS0.2 sample; (c) RS0.6 sample; (d) histogram for the fraction change of the three grains before and after tensile tests. (For interpretation of the references to colour in this figure legend, the reader is referred to the web version of this article).

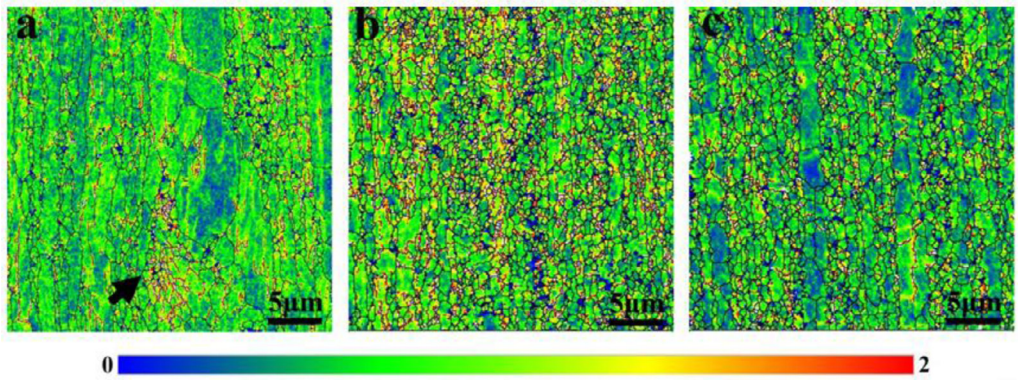

Fig. 12. Kernel average misorientation (KAM) maps of α-Al grains after tensile test at 350 °C: (a) EXT sample; (b) RS0.2 sample; (c) RS0.6 sample, the arrow in (a) indicates the strain localization occurred at the interfaces between the large grains and the small ones.

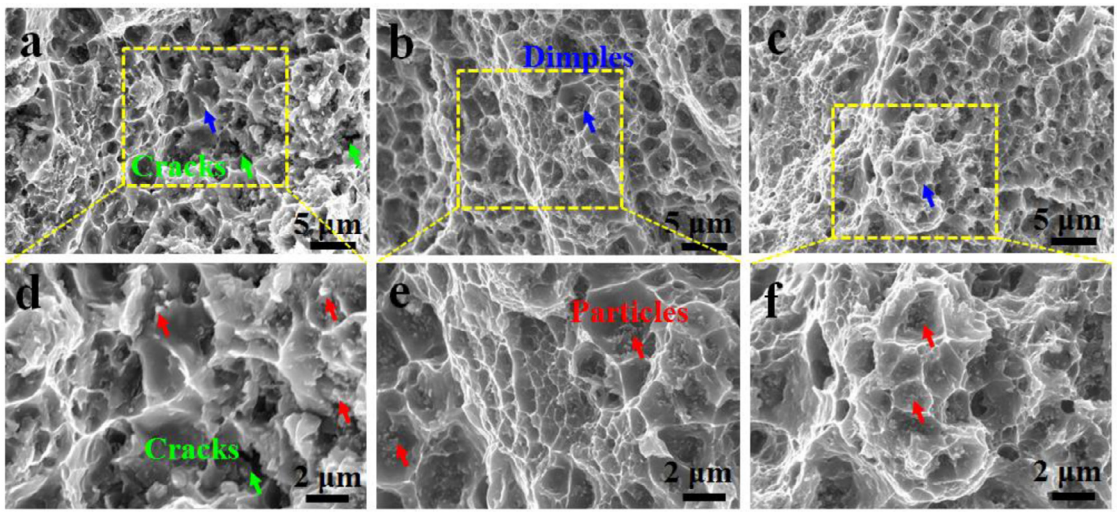

Fig. 13. The tensile fracture surfaces at high temperature at low and high magnifications for the AlN_p/Al composites: (a, d) showing the cracks and dimples on the fracture surfaces of EXT sample; (b, e) showing the dimples on the fracture surface of RS0.2 sample; (c, f) showing the dimples on the fracture surface of RS0.6 sample.

displayed in Fig. 12a, the strain distribution in the matrix is not uniform and strain localization occurs at the interfaces between the large grains and the small ones indicated by the dark arrow, which indicates dislocation pileups in the local area in large quantities. After RS treatment, the strain distribution is more uniform and the strain localization caused by local dislocation pileups becomes more dispersed shown in Figs. 12b and c, which prove that both RS0.2 and RS0.6 samples have been subjected to higher strains during high-temperature loading as compared with its counterpart. Therefore, larger uniform elongation deformation was obtained in the composites after RS along with the variation of the net-work structure of AlN_p.

4.3. Fracture behavior of the composites

It is generally considered that particle clusters in the Al matrix composites result in decreased elongation due to void nucleation and coalescence at interfaces [48], but reduction of the particle size can improve the elongation significantly [49,50]. Besides, the more homogeneous the void distribution in the matrix is, the higher the elongation of the materials will be [51,52]. In a previous work, it is proved that voids are initiated at the interfaces between AlN_p and Al matrix with increasing tensile strain after uniform plastic deformation [9]. Thus, the larger total elongation in the RS treated samples can be attributed to the more dispersive distribution of the AlN_p. Therefore, tailoring the network-structure of AlN_p under a low strain RS deformation is proved beneficial to the improvement of ductility and toughness of the composites. Furthermore, fractography observations were conducted to understand the fracture mechanisms of the composites. Fig. 13 shows fracture surfaces of the three samples after tensile testing at 350 °C. Amounts of dimples in different sizes and characteristics can be observed in tensile fracture surfaces, which indicate ductile fracture mode. As shown in Figs. 13a and d, the dimples on the surfaces of EXT are not uniform, which were caused by the lamellar distribution of particles. Some cracks with sizes of about 2–3 μm can be observed at the interfaces of agglomerated particles as indicated by the yellow arrows, which also suggested severe stress concentration in the sample EXT. After RS treatment, the dimples on the surfaces of RS0.2 and RS0.6 became more uniform and the cracks cannot be observed obviously (Figs. 13b and c). At a higher magnification (Fig. 13d), it is noted the tear ridges are blunt and there are lots of particles exposed on the surfaces as shown by the red arrows, which also reveal that rapid softening of the matrix occurred in the sample EXT. Compared with Fig. 13d, the tear ridges in Figs. 13e and f were much shaper and the average dimple size decreased, indicating that larger plastic strain occurred and the rapid softening was retarded in the RS treated samples. After RS treatment, the matrix grains were refined and the particles in the matrix were dispersed much more uniformly, which hindered the dynamic softening and resulted in the enhancement in the ductility and fracture toughness.

5. Conclusions

In this work, a network-structured AlN_p reinforced Al composite was processed by RS treatment to retard the rapid softening and to improve the strength-ductility synergy at high temperature. It has shown that room temperature RS treatment after the hot extrusion may provide a unique method for fabrication of nanostructured Al based composites exhibiting improved strength-ductility relationships. Specifically, the following conclusions can be drawn:

1. The heterogenous lamellar structure consisting of particle rich zones and elongated α-Al grains of AlN_p/Al matrix composites have been manipulated and the particle distribution becomes much more uniform.
2. The rapid softening of the composites at high temperatures can be retarded after RS treatment. The uniform elongation of the composites increased by 112%, from 0.99% to 2.1%, while the UTS at high temperature is comparable with the unprocessed one and only a slight decrease occurred from 126 MPa to 113 MPa, achieving a good strength and ductility matching.
3. A unique strain hardening retention was achieved, indicating a restored strain hardening after the regulation of the microstructure. Meanwhile, the strain rate sensitivity of the composites was also increased and m value of RS0.6 sample is nearly three times higher for than that of the EXT sample.
4. The restored strain hardening, the higher strain rate sensitivity as well as the restrained strain localization at high temperatures account for the significant improvement of the composites' ductility at 350 °C. While, the pinning effects and load bearing efficiency of the AlN architecture decreased to some extent, leading to the slight loss of tensile strength.

Declaration of Competing Interest

The authors declare that they have no known competing financial interests or personal relationships that could have appeared to influence the work reported in this paper.

Acknowledgements

This work was supported by the National Key R&D Program of China (No. 2017YFA0204403), Key Program of National Natural Science Foundation of China (Nos. 51731007 and 51931003), National Natural Science Foundation of China (Nos. 51971112 and 51501092) and the Fundamental Research Funds for the Central Universities (No. 30919011405). The authors also want to acknowledge the support of the Jiangsu Key Laboratory of Advanced Micro-Nano Materials and Technology. SEM, TEM and EBSD experiments are performed at the Materials Characterization and Research Center of Nanjing University of Science and Technology.

Supplementary materials

Supplementary material associated with this article can be found, in the online version, at doi:10.1016/j.mtla.2019.100523.

References

[1] Z. Wang, R.T. Qu, S. Scudino, B.A. Sun, K.G. Prashanth, J. Eckert, Hybrid nanostructured aluminum alloy with super-high strength, NPG Asia Mater. 7 (2015) 1–8.
[2] P.V. Liddicoat, X.Z. Liao, Y.H. Zhao, Y.T. Zhu, M.Y. Murashkin, E.J. Lavernia, R.Z. Valiev, S.P. Ringer, Nanostructural hierarchy increases the strength of aluminium alloys, Nat. Commun. 1 (2010) 1–7.
[3] J.C. Williams, E.A. Starke, Progress in structural materials for aerospace systems11The golden jubilee issue—selected topics in materials science and engineering: past, present and future, edited by S. Suresh, Acta Mater. 51 (2003) 5775–5799.
[4] M.K. Surappa, Aluminium matrix composites: challenges and opportunities, Sadhana 28 (2003) 319–334.
[5] T. Dursun, C. Soutis, Recent developments in advanced aircraft aluminium alloys, Mater. Des. (1980-2015) 56 (2014) 862–871.
[6] C. Borgonovo, D. Apelian, M.M. Makhlouf, Aluminum nanocomposites for elevated temperature applications, JOM 63 (2010) 57–64.
[7] X.Y. Liu, Q.L. Pan, L.Y. Zheng, Q.R. Fu, F. Gao, M.X. Li, Y.M. Bai, Effect of aging temper on the thermal stability of Al–Cu–Mg–Ag heat-resistant alloy, Mater. Des. 46 (2013) 360–365.
[8] M. Abdulwahab, I.A. Madugu, S.A. Yaro, A.P.I. Popoola, Effects of temper conditions and step-quenching-ageing on the hardness characteristics and yield strength of A356.0-type Al-Si-mg alloy, Silicon 4 (2012) 137–143.
[9] X. Ma, Y.F. Zhao, W.J. Tian, Z. Qian, H.W. Chen, Y.Y. Wu, X.F. Liu, A novel Al matrix composite reinforced by nanoeAlNp network, Sci. Rep. 6 (2016) 34919.
[10] Q.L. Zhao, H.D. Zhang, X.X. Zhang, Q. Feng, Q.C. Jiang, Enhanced elevated-temperature mechanical properties of Al-Mn-Mg containing TiC nano-particles by pre-strain and concurrent precipitation, Mater. Sci. Eng. A 718 (2018) 305–310.
[11] H.B. Yang, T. Gao, G.L. Liu, X.J. Zhao, H.W. Chen, H.C. Wang, J.F. Nie, X.F. Liu, Simultaneously improving strength and ductility for Al–Cu–Mg alloy via threadiness array of TiC nanoparticles, Materials 6 (2019) 100333.
[12] Y.F. Liu, F. Wang, Y. Cao, J.F. Nie, H. Zhou, H.B. Yang, X.F. Liu, X.H. An, X.Z. Liao, Y.H. Zhao, Y.T. Zhu, Unique defect evolution during the plastic deformation of a metal matrix composite, Scr. Mater. 162 (2019) 316–320.
[13] C. Poletti, M. Balog, F. Simancik, H.P. Degischer, High-temperature strength of compacted sub-micrometer aluminium powder, Acta Mater. 583 (2010) 781–789.
[14] S.D. Liu, K.K. Chang, S. Mráz, X. Chen, M. Hans, D. Music, D. Primetzhofer, J.M.M. Schneider, Modeling of metastable phase formation for sputtered $Ti_{1-x}Al_xN$ thin films, Acta Mater. 165 (2019) 615–625.
[15] A.W. Zhu, A. Csontos, E.A. Starke, Computer experiment on superposition of strengthening effects of different particles, Acta Mater. 47 (1999) 1713–1721.
[16] L.Y. Chen, J.Q. Xu, H. Choi, M. Pozuelo, X.L. Ma, S. Bhowmick, J.M. Yang, S. Mathaudhu, X.C. Li, Processing and properties of magnesium containing a dense uniform dispersion of nanoparticles, Nature 528 (2015) 539–543.
[17] N. Ramakrishnan, An analytical study on strengthening of particulate reinforced metal matrix composites, Acta Mater. 44 (1996) 69–77.
[18] A. Mortensen, J. Llorca, Metal matrix composites, Annu. Rev. Mater. Res. 40 (2010) 243–270.
[19] Q. Zhang, G.Q. Chen, G.H. Wu, Z.Y. Xiu, B.F. Luan, Property characteristics of a Aln_p/Al composite fabricated by squeeze casting technology, Mater. Lett. 57 (2003) 1453–1458.
[20] K.B. Lee, H.S. Sim, S.W. Heo, H.R. Yoo, S.Y. Cho, H. Kwon, Tensile properties and microstructures of Al composite reinforced with Bn particles, Compos. Part A Appl. Sci. Manuf. 33 (2002) 709–715.
[21] J.C. Li, X.X. Zhang, L. Geng, Improving graphene distribution and mechanical properties of GNP/Al composites by cold drawing, Mater. Des. 144 (2018) 159–168.
[22] Z. Hashin, S. Shtrikman, A variational approach to the theory of the elastic behaviour of multiphase materials, J. Mech. Phys. Solids 11 (1963) 127–140.
[23] L.J. Huang, L. Geng, H.X. Peng, Microstructurally inhomogeneous composites: is a homogeneous reinforcement distribution optimal? Prog. Mater. Sci. 71 (2015) 93–168.
[24] I. Sabirov, O. Kolednik, R.Z. Valiev, R. Pippan, Equal channel angular pressing of metal matrix composites: effect on particle distribution and fracture toughness, Acta Mater. 53 (2005) 4919–4930.
[25] Y. Yang, J.F. Nie, Q.Z. Mao, Y.H. Zhao, improving the combination of electrical conductivity and tensile strength of Al 1070 by rotary swaging deformation, Result Phys. 13 (2019) 102236.
[26] M.A. Abdulstaar, E.A. El-Danaf, N.S. Waluyo, L. Wagner, Severe plastic deformation of commercial purity aluminum by rotary swaging: microstructure evolution and mechanical properties, Mater. Sci. Eng. A 565 (2013) 351–358.
[27] M. Shahzad, Influence of Extrusion Parameters on Microstructure Development and Mechanical Properties in Wrought Magnesium Alloys AZ80 and ZK60 Dr.-Ing. Thesis, TU Clausthal, 2007.
[28] X. Ma, Y.F. Zhao, X.J. Zhao, T. Gao, H.W. Chen, X.F. Liu, Influence mechanisms of Cu or Fe on the microstructures and tensile properties at 350 °C of network AlNp reinforced Al composites, J. Alloys Compd. 740 (2018) 452–460.
[29] M.A. Abdulstaar, E.A. El-Danaf, N.S. Waluyo, L. Wagner, Severe plastic deformation of commercial purity aluminum by rotary swaging: microstructure evolution and mechanical properties, Mater. Sci. Eng. A 565 (2013) 351–358.
[30] Radim Kocich, Lenka Kunčická, Petr Král, Pavel Strunz, Characterization of innovative rotary swaged Cu-Al clad composite wire conductors, Mater. Des. 160 (2018) 828–835.
[31] B. Beausir, J.-.J. Fundenberger, Analysis Tools for Electron and X-ray diffraction, ATEX - software, Université de Lorraine - Metz, 2017 www.atex-software.eu.
[32] J.W. Hutchinson, K.W. Neale, Influence of strain-rate sensitivity on necking under uniaxial tension, Acta Metall. 25 (1977) 839–846.
[33] Y.T. Zhu, X.L. Wu, Ductility and plasticity of nanostructured metals: differences and issues, Mater. Today Nano 2 (2018) 15–20.
[34] Y.M. Wang, E. Ma, Strain hardening, strain rate sensitivity, and ductility of nanostructured metals, Mater. Sci. Eng. A 375–377 (2004) 46–52.
[35] M. Dao, L. Lu, Y.F. Shen, S. Suresh, Strength, strain-rate sensitivity and ductility of Cu with nano-scale twins, Acta Mater. 54 (2006) 5421–5432.
[36] L. Lu, M. Dao, T. Zhu, J. Li, Size dependence of rate-controlling deformation mechanisms in nanotwinned copper, Scr. Mater. 60 (2009) 1062–1066.
[37] M.D. Gram, J.S. Carpenter, P.M. Anderson, An indentation-based method to determine constituent strengths within nanolayered composites, Acta Mater. 92 (2015) 255.
[38] X.L. Wu, P. Jiang, L. Chen, F.P. Yuan, Y.T. Zhu, Extraordinary strain hardening by gradient structure, PNAS 111 (2014) 7197–7201.
[39] M.X. Yang, Y. Pan, F.P. Yuan, Y.T. Zhu, X.L. Wu, Back stress strengthening and strain hardening in gradient structure, Mater. Res. Lett. 4 (2016) 145–151.

[40] Q. Wei, S. Cheng, K.T. Ramesh, E. Ma, Effect of nanocrystalline and ultrafine grain sizes on the strain rate sensitivity and activation volume: fcc versus bcc metals, Mater. Sci. Eng. A 381 (2004) 71–79.
[41] J. Chen, L. Lu, K. Lu, Hardness and strain rate sensitivity of nanocrystalline Cu, Scr. Mater. 54 (2006) 1913–1918.
[42] M. Dao, L. Lu, R.J. Asaro, J.T.M. De Hosson, E. Ma, Toward a quantitative understanding of mechanical behavior of nanocrystalline metals, Acta Mater. 54 (2007) 4041–4065.
[43] L. Blaza, P. Lobry, M. Zygmunt-Kiper, J. Koziel, G. Wloch, S. Dymek, strain rate sensitivity of Al-based composites reinforced with MnO_2 additions, J. Alloys Compd. 619 (2015) 652–658.
[44] M. Kawasaki, T.G. Langdon, Review: achieving superplastic properties in ultrafine–grained materials at high temperatures, J. Mater. Sci. 51 (2016) 19–32.
[45] Y.J. Wei, Y.Q. Li, L.C. Zhu, Y. Liu, X.Q. Lei, G. Wang, Y.X. Wu, Z.L. Mi, J.B. Liu, H.T. Wang, H.J. Gao, Evading the strength–ductility trade-off dilemma in steel through gradient hierarchical nanotwins, Nat. Commun. 5 (2014) 3580.
[46] S. Whalen, M. Olszta, C. Roach J. Darsell, D. Graff, M. Reza-E-Rabby, T. Roosendaal, W. Daye, T. Pelletiers, S. Mathaudhu, N. Overman, High ductility aluminum alloy made from powder by friction extrusion, Materials 6 (2019) 100260.
[47] J. Liu, Z. Chen, F.G. Zhang, G. Ji, M.L. Wang, Y. Ma, V. Ji, S.Y. Zhong, Y. Wu, H.W. Wang, Simultaneously increasing strength and ductility of nanoparticles reinforced al composites via accumulative orthogonal extrusion process, Mater. Res. Lett. 6 (2018) 406–412.
[48] J. Lewandowski, C. Liu, W. Hunt Jr., Effects of matrix microstructure and particle distribution on fracture of an aluminum metal matrix composite, Mater. Sci. Eng.: A 107 (1989) 241–255.
[49] M.K. Akbari, H. Baharvandi, K. Shirvanimoghaddam, Tensile and fracture behavior of nano/micro TiB2 particle reinforced casting A356 aluminum alloy composites, Mater. Des. 66 (2015) 150–161.
[50] M. Rahimian, N. Parvin, N. Ehsani, Investigation of particle size and amount of alumina on microstructure and mechanical properties of al matrix composite made by powder metallurgy, Mater. Sci. Eng. A 527 (4–5) (2010) 1031–1038.
[51] K. Kannan, C.H. Hamilton, Cavity distribution effects on superplastic ductility of a eutectic Pb-Sn alloy, Scr. Mater. 37 (1997) 455–462.
[52] M.B. Taylor, H.M. Zbib, M.A. Khaleel, Damage and size effect during superplastic deformation, Int. J. Plast. 18 (2002) 415–442.